An implicit time marching Galerkin method for the simulation of icing phenomena with a triple layer model

Rémi Chauvin, L. Bennani, P. Trontin, P. Villedieu

An Implicit Time Marching Galerkin Method for the Simulation of Icing Phenomena with a Triple Layer Model

R.Chauvin[a], L.Bennani[b,*], P.Trontin[b], P.Villedieu[b]

[a] *CEA/DAM/DIF, Chemin du Ru, 91680 Bruyères-le-Châtel, France*
[b] *ONERA/DMPE, Université de Toulouse, F-31055 Toulouse - France*

Abstract

In the context of more electrical aircraft and reduction of fuel consumption, aircraft manufacturers are moving towards more complex and transient ice protection systems. The operating of these systems involves several unsteady heat and mass transfer phenomena. Modelling and numerical simulation play an important role in the investigation of these unsteady phenomena. In this paper, a model for unsteady ice build-up and melting is presented. The model is based on a triple layer assumption. In addition, a tailored numerical methodology for solving the governing partial differential equations is also described. It is based on a Galerkin finite element method and a Gauss-Seidel like implicit time marching scheme. The global method is validated and its capabilities are demonstrated on several cases.

Keywords: icing; triple layer; finite element method; runback; modelling; numerical simulation

Nomenclature

$\frac{\partial p}{\partial x}$	Aerodynamic tangential pressure gradient $[N.m^{-3}]$
Γ_k	Mass transfer term for the k-th layer $[kg.m^{-2}.s^{-1}]$
$\hat{T}_f$	Mean temperature of the running liquid film $[K]$
$\hat{v}_x$	Mean velocity of the running liquid film $[m.s^{-1}]$
λ_k	Thermal conductivity of the material in layer k $[W.m^{-1}.K^{-1}]$
μ_w	Viscosity of water $[Pa.s]$
Φ_f	Energy transfer term for the liquid running film $[J.m^{-2}.s^{-1}]$
ρ_k	Density of the material in layer k $[kg.m^{-3}]$
τ	Aerodynamic shear stress $[N.m^{-2}]$
a_k	Position of the lower boundary of the k-th layer in the z direction $[m]$
b_k	Position of the upper boundary of the k-th layer in the z direction $[m]$
c_k	Specific heat of the material in layer k $[J.kg^{-1}.K^{-1}]$
g_x	Gravity component along the curvilinear direction $[m.s^{-2}]$

*Corresponding author
Email addresses: remi.chauvin@cea.fr (R.Chauvin), lokman.bennani@onera.fr (L.Bennani), pierre.trontin@onera.fr (P.Trontin), philippe.villedieu@onera.fr (P.Villedieu)

h_f Running liquid film thickness $[m]$

T_k Temperature field in the k-th layer $[K]$

α Angle of attack $[°]$

$\dot{m}_{ev}(T)$ Rate of evaporation at temperature T $[kg.s^{-1}]$

$\dot{m}_{ice,bottom}$ Liquid/solid phase change rate at the bottom surface of an ice block $[kg.s^{-1}]$

$\dot{m}_{ice,top}$ Liquid/solid phase change rate at the top surface of an ice block $[kg.s^{-1}]$

$\dot{m}_{imp}$ Rate of impacting droplets $[kg.s^{-1}]$

$\dot{m}_{in}$ Mass flow rate of running liquid film entering a cell $[kg.s^{-1}]$

$\dot{m}_{out}$ Mass flow rate of running liquid film exiting a cell $[kg.s^{-1}]$

$\dot{m}_s(T)$ Rate of sublimation at temperature T $[kg.s^{-1}]$

Ψ_j j-th basis function for the Galerkin method

$\theta_{k,j}$ j-th Galerkin degree of freedom associated to the k-th layer $[K]$

L_f Latent heat of fusion $[J.kg^{-1}]$

L_s Latent heat of sublimation $[J.kg^{-1}]$

L_v Latent heat of vaporization $[J.kg^{-1}]$

M_∞ Freestream Mach number

MVD Mean Volumetric Diameter $[\mu m]$

P_∞ Freestream pressure $[Pa]$

rH_∞ Freestream relative humidity

T_∞ Freestream temperature $[K]$

T_{fe} Skin temperature in the full evaporative case $[K]$

T_{imp}^{tot} Total temperature of impacting droplets $[K]$

TWC Total Water Content $[g.m^{-3}]$

1. Introduction

Ever since the pioneering days of flight, the icing phenomenon, or the "ice problem" as it was called in the early days, has been reckognized as a serious threat [30, 31]. Typical icing conditions are due to the presence in clouds of supercooled water droplets. Upon impacting an aircrafts surface, the metastable supercooled state of the droplets is broken. At that point, the droplets undergo a liquid-solid phase change, leading to ice bluid-up on the impinged surface. Increased mass, degradation of aerodynamic performances and handling qualities or blocked air intakes, those are some of the many undesirable consequences one has to face when dealing with icing. Indeed, in the aeronautical world, icing is one of the most serious hazards that can be encountered.

Aircraft manufacturers must therefore comply with certifications and regulations regarding flight safety in icing conditions. In order to achieve that goal, several ice protection technologies may be used. A commonly

employed system for large airliners is the bleed-air anti-icing system. However, in the context of more electrical aircraft and reduction of fuel consumption, alternative systems are currently under consideration for large airliners. The main idea is to use a system which would be able to function in de-icing mode. That is to say that a reasonable amount of ice is allowed to build up. Periodically, the system is activated and the ice is shed from the surface or melted. Such a system would have an unsteady cyclic operating mode, enabling a more optimized use of energy. These systems operate in complex environments and involves many physical processes. In order to study such systems and assist their design phase, models and numerical simulation methodologies are an important asset.

Historically, one of the first models devised to study ice build up on a surface was Messinger's model [17]. It has served as the basis for many icing simulation tools [12, 23, 14, 26, 13, 32] and is still in wide use to this day.

However, it is a steady state model and is not well suited if one wishes to take into account the interaction with an unsteady system. Moreover, an important underlying hypothesis to the model is that the temperature does not vary in the ice block in the direction normal to the surface. As a consequence the heat fluxes are not taken into account and the model is not well suited to applications involving ice protection systems. For example, Messinger's model is not able to capture the melting dynamics of an ice block when an ice protection system is activated. In addition, the operating of ice protection systems can involve freezing runback films which are not well accounted for by Messinger's model.

In order to model and simulate unsteady icing phenomena, several issues must be addressed. First, one must account for the dynamics of the liquid film. This issue has been studied by many researchers. For example, Al-Khalil et al. have proposed a macroscopic runback model applied to the study anti-icing systems [1]. In addition, Tsao and Rothmayer have performed theoretical work using matched asymptotic expansions [28, 27]. In particular, their analysis gives a possible explanation to the formation of roughness at the surface of glaze ice. Furthermore, in order to perform unsteady simulations, Bourgault et al. proposed an unsteady three dimensional ice accretion model based on a lubrication theory assumption [6]. Although more sophisticated approaches have been developed and researched [21, 10], lubrication theory is still widely used and sufficient for most applications [29, 16].

Secondly, one must take into account the unsteady heat and mass transfer phenomena. To do so, Myers has proposed to extend Messinger's model by using a multi-layered approach (one layer of ice and two layers of liquid water) [18, 20]. In each layer, a linear temperature profile is assumed (in the direction normal to the surface) and the evolution of the temperature field is treated in a quasi-steady framework. These ideas were used in more recent work in a quasi-steady framework [29, 33, 11]. Later, Myers et al. extended this idea to unsteady one dimensional cases by assuming a cubic temperature profile in each layer [19]. The cases addressed in [19] were of fixed total thickness. Phenomena such as evaporation or ice build up due to impacting droplets were not treated. Moreover, the problem of creation/vanishing of a layer was not addressed.

The goal of the present work is to extend the previously mentioned research to develop a unified model and numerical method, enabling to take into account all unsteady phenomena encountered during ice build-up on a surface (eventually heated by a system). The proposed approach allows to take into account the necessary unsteady physics (water runback, dynamic phase change interfaces, unsteady temperature fields, creation/vanishing of a layer, etc) while remaining computationally tractable. Moreover, the method allows numerical coupling with simulation tools for thermal ice protection systems.

The present paper is articulated as follows. In the first section, the general context of the approach is presented. After that, the main physical models, which constitute the building blocks of the three-layer approach, are introduced. Then, the spatial finite element discretization and implicit time marching scheme are described. Finally, some validations and applications of the method are shown.

2. General Context

The simulation of icing phenomena in aeronautics involves several coupled physical phenomena. State of the art icing codes are articulated around specialized modules which are coupled during the computation.

For example, a widely used approach to compute an ice shape is illustrated in Figure 1. An inviscid flow solver is used to obtain the external flow field. This field is used as an input for a droplet trajectory module and a boundary layer module. These two modules in turn provide the inputs for the ice accretion module.

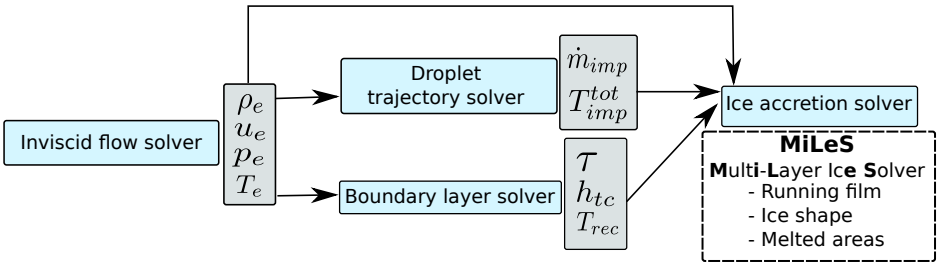

Figure 1: State of the art icing code architecture. The work presented in this paper focuses on the ice accretion solver.

As stated earlier, classic ice accretion solvers are based on Messinger's model. The idea is to partition the airfoil into cells and to consider each cell as an open thermodynamic system. The equations of conservation of mass and energy in steady state are solved, but by considering a uniform state on the cell. As shall be described in the rest of the paper, the model introduced here is unsteady and considers three layer so as to account for the running film dynamics and the temperature gradients within the ice and the melted water regions.

The work presented here is focused on the 'ice accretion solver' block of Figure 1. The unsteady ice accretion solver is called MiLeS and its numerical implementation is part of a larger simulation framework, developed at ONERA, called IGLOO2D and IGLOO3D [22, 24]. In what follows, the model and numerical method will be presented in a two dimensional framework.

As shown in Figure 1, the inputs of the ice accretion solver are the (local) droplet impingement rate noted $\dot{m}_{imp}$, their total temperature T^{tot}_{imp}, the heat transfer coefficient h_{tc}, the recovery temperature T_{rec}, the shear stress τ and the inviscid flow quantities. The ice accretion solver outputs the local running film height, height of ice, height of melted water and the temperature fields in each layer.

3. Physical Model of MiLeS2D

In order to construct the three-layer model, let us consider the illustrative icing situation shown in Figure 2. In this situation, the physical process may be described by considering six distinct modes (labeled $1-6$ in Figure 2):

1. Full evaporative: the whole mass of impacting droplets is evaporated (for example, due to heat provided by an ice protection system).
2. Running wet: only a liquid water film is present. Under the action of the aerodynamic forces, the liquid film runs back along the surface.
3. Rime accretion: the droplets freeze almost instantaneously leading to ice build up with no liquid water.
4. Glaze accretion: the droplets freeze, but at a slower rate than in the rime case. Therefore, a running liquid water film is present on top of the ice layer.
5. Rime accretion with melting at the surface (due to heat provided by an ice protection system for example).
6. Glaze accretion with melting at the surface (due to heat provided by an ice protection system for example).

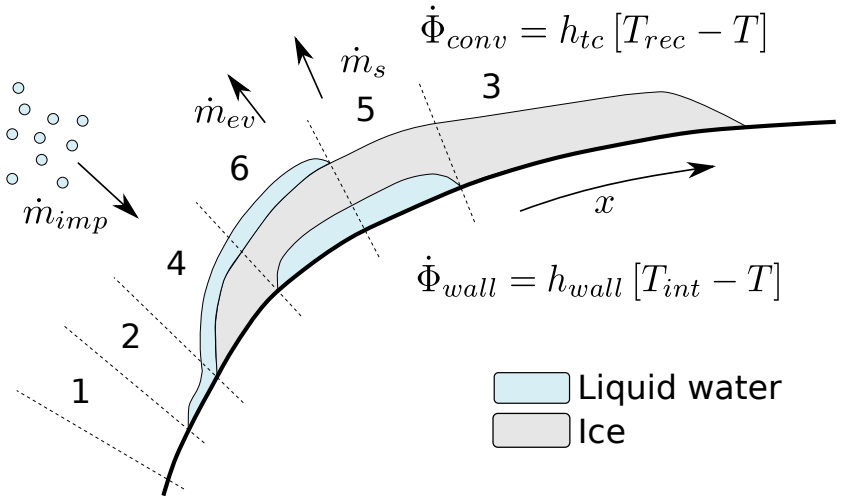

Figure 2: Illustration of a generic icing situation

In each mode, one can distinguish the presence (or abscence) of one or more layers. The term *three-layer model* comes from the fact that in the most general case one has to deal with three layers:

1. Running film: this is the water layer directly in contact with the airflow. It is sheared by the aerodynamic flow and runs back downstream.
2. Ice: this layer represents the ice that may build up in icing conditions.
3. Static film: when a system is activated, a part of the ice layer may melt. This has the effect of forming a static film layer (it is not in contact with the external aerodynamic flow).

The three layers, as well as some geometric quantities which characterize them, are represented in Figure 3. Subscript f is used to denote the running film layer, i for the ice layer and s for the static film layer. For each layer k ($k = i, s$), a_k is the position of the lower boundary and b_k is the position of the upper boundary (in the z direction, normal to the surface).

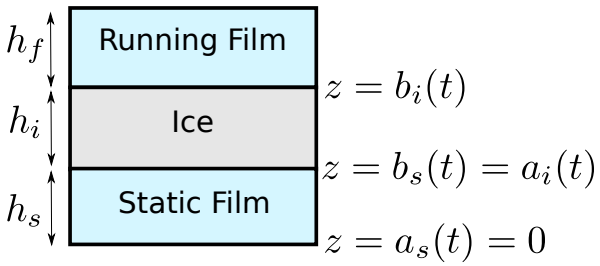

Figure 3: Illustration of the three layers: h_f, h_i and h_s are the heights of the running film, ice and static (melted) film. The a_k's and b_k's represent the positions of the boundaries between each layer in the z direction (normal to the surface)

The whole model may be fully expressed in terms of PDEs [7]. However, this requires to consider each mode shown in Figure 2 because specific boundary conditions and source terms correspond to each one. In order to present the approach in a more concise way, while not losing much in generality, it shall be presented as follows. First, the main equations used to model heat and mass transfer will be presented. Secondly, the ways of combining them to describe each of the six modes are given with the corresponding set of boundary conditions and source terms. Then, in the following section, the spatial discretization will be presented. Finally, the implicit time integration scheme is described.

3.1. Equations for the running film layer

In order to obtain an unsteady formulation, the dynamics of the liquid film need to be modelled. The unknowns are the film thickness h_f and the mean temperature $\hat{T}_f$. To do so, as the film is very thin, an integral approach is used combined with a closure relation from lubrication theory [7].

In the framework of lubrication theory, the mean velocity of the running liquid ($\hat{v}_x$) only depends on its thickness h_f and the external flow conditions:

$$\hat{v}_x(h_f) = \frac{\tau}{2\mu_w} h_f + \frac{1}{3\mu_w}\left(-\frac{\partial p}{\partial x} + \rho_w g_x\right) h_f^2 \tag{1}$$

where τ is the air shear stress, $\frac{\partial p}{\partial x}$ is the tangential pressure gradient and g_x is the tangential gravity. In this framework, surface tension and wettability effects are neglected.

One obtains the following system of PDEs:

- Mass conservation

$$\frac{\partial \rho_w h_f}{\partial t} + \frac{\partial \rho_w h_f \hat{v}_x}{\partial x} = \Gamma_f \tag{2}$$

  where Γ_f is the mass transfer term (which will be detailed later and is specific to each mode).

- Energy conservation: as the liquid film is very thin, the temperature profile is assumed uniform in the normal direction. The energy equation is given by:

$$\frac{\partial \rho_w c_w h_f \hat{T}_f}{\partial t} + \frac{\partial \rho_w c_w h_f \hat{v}_x \hat{T}_f}{\partial x} = \dot{\Phi}_f \tag{3}$$

  where $\dot{\Phi}_f$ is the energy transfer term (which will be detailed later and is specific to each mode).

  In the case where the liquid film is (locally) running over ice, equation (3) degenerates to $\hat{T}_f = T_m$. Indeed, at an interface between running film and ice, phase change is occurring. Hence the temperature at the interface is the melting temperature. As the liquid film is assumed to be very thin and of uniform temperature on the normal direction, the whole film is at the melting temperature.

3.2. Heat conduction in the ice layer and melted film layer

Both the ice and melted film layers are assumed motionless. Here, the subscript k will be used to generically denote these two layers ($k = i$ or $k = s$). Furthermore, heat transfer in the tangential direction is neglected (see Appendix A for an assessment of this approximation). Heat transfer is considered in the z (normal) direction only.

- Mass conservation (at each curvilinear abscissa x):

$$\frac{\partial \rho_k h_k}{\partial t} = \Gamma_k \tag{4}$$

  where Γ_k is the mass transfer term (which will be detailed later).

- Energy conservation (at each curvilinear abscissa x)

$$\begin{aligned}
\frac{\partial \rho_k c_k T_k}{\partial t} &= \lambda_k \frac{\partial^2 T_k}{\partial z^2} && \text{For } z \text{ in }]a_k(t), b_k(t)[\\
f_a\left(T_k, \frac{\partial T_k}{\partial z}\right) &= 0 && \text{For } z = a_k(t) \\
f_b\left(T_k, \frac{\partial T_k}{\partial z}\right) &= 0 && \text{For } z = b_k(t)
\end{aligned} \tag{5}$$

  where for each layer $k = i$ or s, ρ_k is the density, c_k the specific heat and T_k the temperature. f_a and f_b denote in a generic way the boundary conditions at the moving boundaries of each layer, as explained in the next paragraph.

3.3. The six modes: boundary conditions, source terms and coupling between layers

In the previous subsection, the main governing equations for each layer (running film, ice or static film) were described. In order to obtain a complete model, these equations are combined so as to describe the six possible modes shown in Figure 2.

Before describing each mode, let us first discuss some general aspects. The convective heat transfer with the outer boundary layer and internal surface heating are independent of any given mode. The convective heat transfer flux is given by the relation:

$$\dot{\Phi}_{conv}(T) = h_{tc}\,[T_{rec} - T] \tag{6}$$

where h_{tc} is the boundary layer heat transfer coefficient and T_{rec} is the recovery temperature. They are inputs of the model.

The heating flux at the lower boundary is given by

$$\dot{\Phi}_{wall}(T) = h_{wall}\,[T_{int} - T] + \dot{\Phi}_0 \tag{7}$$

where h_{wall} is the wall heat transfer coefficient, T_{int} is the temperature on the inside of the surface and $\dot{\Phi}_0$ a given flux (in the case of a Neumann condition for example). These are again inputs of the model.

In what follows, $\dot{m}_{ev}$ denotes the evaporation mass rate and $\dot{m}_s$ the sublimation mass rate. They are both computed using the Chilton-Colburn analogy [9].

At interfaces where phase change occurs the rate of phase change is governed by a Stefan condition. For example, at the interface between the ice and the static water layers, $\dot{m}_{ice}$ (rate of phase change of the ice layer) is given by:

$$\dot{m}_{ice} L_m = \lambda_w \left.\frac{\partial T_s}{\partial z}\right|_{interface} - \lambda_i \left.\frac{\partial T_i}{\partial z}\right|_{interface} \tag{8}$$

In addition, recall that the temperature profile in the running film is assumed to be uniform. In the modes were a liquid running film layer is present, the computation of the temperature gradient in the running liquid film layer is not possible. However, this term is required in order to compute the rate of melting/freezing (governed by the Stefan condition as just stated). So as to overcome this limitation, the temperature gradient is also assumed constant (and different from zero) as if the temperature profile was in fact linear.

Note that the uniform temperature and constant gradient assumptions are not incompatible in the present case. The uniform temperature assumption is a closure hypothesis for the energy equation for the running film [7]. It is a reasonable assumption given the small characteristic thickness of the running film in the targeted applications of this work. The characteristic thickness of the running film is of a few microns. A temperature difference of $0.1K$ across the film thickness, which is coherent with a uniform temperature assumption, would yield a temperature gradient of $10^5 K/m$ (assuming a linear profile). Therefore, the uniform temperature and constant gradient assumptions are coherent (in our context).

When the heat flux at the running film/ice interface is required, it is computed by assuming that it is equal to the heat flux at the upper boundary of the running film. This is used for example in equation (17) for the glaze mode.

We now proceed to the description of each mode and their specific boundary conditions, source terms and coupling terms.

1 - Full evaporative

In this mode, the whole quantity of water in the cell is evaporated. No layer is present in this mode. The unknown is the temperature at the wall T_{fe}. The full evaporative case is governed by equations (2) and (3) with $h_f = 0$, $\frac{\partial \rho_w h_f}{\partial t} = 0$ and $\frac{\partial \rho_w c_w h_f \hat{T}_f}{\partial t} = 0$. The source terms for (2) and (3) are given by:

$$\Gamma_{fe} = \dot{m}_{imp} - \dot{m}_{ev}(\hat{T}_{fe}) \tag{9}$$

$$\dot{\Phi}_{fe} = \dot{m}_{imp} c_w \left[T_{imp}^{tot} - T_{fe}\right] - \dot{m}_{ev}(\hat{T}_{fe}) L_v(T_{fe}) + \dot{\Phi}_{conv}(T_{fe}) + \dot{\Phi}_{wall}(T_{fe}) \tag{10}$$

2 - Running wet

In this mode, only the liquid running film layer is present. The unknowns are the running liquid film height h_f and the mean film temperature $\hat{T}_f$. The source terms for (2) and (3) are given by:

$$\Gamma_f = \dot{m}_{imp} - \dot{m}_{ev}(\hat{T}_f) \tag{11}$$

$$\dot{\Phi}_f = \dot{m}_{imp} c_w T_{imp}^{tot} + \dot{m}_{ev}(\hat{T}_f) \left[c_w \hat{T}_f - L_v(\hat{T}_f)\right] + \dot{\Phi}_{conv}(\hat{T}_f) + \dot{\Phi}_{wall}(\hat{T}_f) \tag{12}$$

3 - Rime accretion

This mode corresponds to the case where all the water arriving in the cell freezes instantaneously. The unknowns are the ice layer height h_i and the temperature field in the ice T_i. The equations describing this mode are (4) and (5). The source terms and boundary conditions are:

$$\Gamma_i = \dot{m}_{imp} - \dot{m}_s(T_i(h_i)) - \frac{\partial \rho_w h_f \hat{v}_x}{\partial x} \tag{13}$$

$$-\lambda_i \left.\frac{\partial T_i}{\partial z}\right|_{z=0} = h_{wall}\left[T_{wall} - T_i(0)\right] + \dot{\Phi}_0 \tag{14}$$

$$\begin{aligned} \lambda_i \left.\frac{\partial T_i}{\partial z}\right|_{z=h_i} =& h_{tc}\left[T_{rec} - T_i(h_i)\right] - \dot{m}_s(T_i) L_s(T_i) \\ &+ \dot{m}_{imp}\left[c_w\left[T_d^{tot} - T_m\right] - c_i\left[T_i(h_i) - T_m\right] + L_f\right] \\ &- \frac{\partial \rho_w c_w h_f \hat{v}_x (\hat{T}_f - T_m)}{\partial x} - \frac{\partial \rho_w h_f \hat{v}_x}{\partial x}\left[c_i\left[T_i(h_i) - T_m\right] + L_f\right] \end{aligned} \tag{15}$$

where the two last terms of equation (15) represent respectively the energy flux brought by the running film and the energy accounting for the freezing of this mass of water.

4 - Glaze accretion

This mode describes the case where an ice layer is present with a liquid running film on top. The unknowns are h_f, h_i, and T_i. As in this mode, there is a liquid layer on top of the ice layer, equation (3) degenerates to $\hat{T}_f = T_m$. This mode is governed by equations (2), (4) and (5) with the following source terms and boundary conditions:

$$\Gamma_f = \dot{m}_{imp} - \dot{m}_{ev}(T_m) - \dot{m}_{ice,top} \tag{16}$$

where $\dot{m}_{ice,top}$ is the rate of phase change at the interface between the running liquid film and the ice.

$$\begin{aligned} \dot{m}_{ice,top} L_m = \lambda_i \left.\frac{\partial T_i}{\partial z}\right|_{z=h_i} - \Big[&\dot{m}_{imp} c_w \left[T_{imp}^{tot} - T_m\right] + \dot{\Phi}_{conv} - \dot{m}_{ev}(T_m) L_v(T_m) \\ &- \frac{\partial \rho_w c_w h_f \hat{v}_x \hat{T}_f}{\partial x}\Big] \end{aligned} \tag{17}$$

where the last four terms are due to the uniform temperature gradient assumption in the running film

flowing over a block of ice.

$$\Gamma_i = \dot{m}_{ice,top} \tag{18}$$

$$T_i(h_i) = T_m \tag{19}$$

$$-\lambda_i \left.\frac{\partial T_i}{\partial z}\right|_{z=0} = h_{wall}\left[T_{wall} - T_i(0)\right] + \dot{\Phi}_0 \tag{20}$$

5 - Rime accretion with static film

In this mode, two static layers are present, the ice layer and a static melted film layer. The unknowns are h_i, T_i, h_s and T_s. This mode is governed by equations (4) and (5) with the following source terms and boundary conditions:

$$\Gamma_i = \dot{m}_{imp} - \dot{m}_s(T_i(h_s + h_i)) + \dot{m}_{ice,bottom} - \frac{\partial \rho_w h_f \hat{v}_x}{\partial x} \tag{21}$$

where $\dot{m}_{ice,bottom}$ is the rate of phase change at the interface between the static layer and the ice.

$$\dot{m}_{ice,bottom} L_m = \lambda_w \left.\frac{\partial T_s}{\partial z}\right|_{z=h_s} - \lambda_i \left.\frac{\partial T_i}{\partial z}\right|_{z=h_s} \tag{22}$$

$$T_i(h_s) = T_m \tag{23}$$

$$\begin{aligned}\lambda_i \left.\frac{\partial T_i}{\partial z}\right|_{z=h_s+h_i} =& h_{tc}\left[T_{rec} - T_i(h_i)\right] - \dot{m}_s(T_i)L_s(T_i) \\ &+ \dot{m}_{imp}\left[c_w\left[T_d^{tot} - T_m\right] - c_i\left[T_i(h_i) - T_m\right] + L_f\right] \\ &- \frac{\partial \rho_w c_w h_f \hat{v}_x (\hat{T}_f - T_m)}{\partial x} - \frac{\partial \rho_w h_f \hat{v}_x}{\partial x}\left[c_i\left[T_i(h_i) - T_m\right] + L_f\right]\end{aligned} \tag{24}$$

$$\Gamma_s = -\dot{m}_{ice,bottom} \tag{25}$$

$$-\lambda_s \left.\frac{\partial T_s}{\partial z}\right|_{z=0} = h_{wall}\left[T_{wall} - \theta_{s,1}\right] + \dot{\Phi}_0 \tag{26}$$

$$T_s(h_s) = T_m \tag{27}$$

6 - Glaze accretion with static film

This is the three-layer mode, a film is running on top of an ice layer with a static melted film layer underneath. The unknowns are h_f, h_i, T_i, h_s and T_s. This mode is governed by equations (2), (4) and (5) with the following source terms and boundary conditions:

$$\Gamma_f = \dot{m}_{imp} - \dot{m}_{ev}(\hat{T}_f) - \dot{m}_{ice,top} \tag{28}$$

$$\Gamma_i = \dot{m}_{ice,top} - \dot{m}_{ice,bottom} \tag{29}$$

$$T_i(h_s + h_i) = T_m \tag{30}$$

$$T_i(h_s) = T_m \tag{31}$$

$$\Gamma_s = -\dot{m}_{ice,bottom} \tag{32}$$

$$-\lambda_s \left.\frac{\partial T_s}{\partial z}\right|_{z=0} = h_{wall}\left[T_{wall} - T_s(0)\right] + \dot{\Phi}_0 \tag{33}$$

$$T_s(h_s) = T_m \tag{34}$$

4. Numerical Method

The next step is to discretize the problem at hand so as to numerically obtain a solution. The spatial discretization is performed as follows:

i The airfoil is discretized into N_x control volumes.

ii Using this x-wise mesh, the spatial derivatives in equations (2) and (3) are discretized with a finite volume Roe scheme [25]. Moreover, in order to obtain a scheme enforcing the maximum principle, a method inspired by the one proposed by Larrouturou is used [15]. These schemes are well established and will not be described in further detail.

iii The z-wise derivatives in the (eventual) ice layer or static film layer are discretized using a Galerkin method.

In the following subsections, the spatial discretization for the heat equation and the implicit time integration scheme are described.

4.1. Finite element spatial discretization in the z direction for the heat equation

If in a given mode, the cell contains an ice layer and/or a static film layer, the heat equation (5) needs to be solved. The main difficulty here is that this equation is written in a moving interface domain delimited by $a_k(t)$ and $b_k(t)$. The change in boundary position is due to phase change phenomena, impingement and evaporation.

The first step is to write the variational formulation of (5). To do so, let $v(z)$ be a test function. The variational formulation of (5) reads:

$$\int_{a_k}^{b_k} \rho_k c_k \frac{\partial T_k}{\partial t} v \, dz - \int_{a_k}^{b_k} \lambda_k \frac{\partial^2 T_k}{\partial z^2} v \, dz = 0 \tag{35}$$

The second step of this method is to introduce the change of variables:

$$\bar{z}(t,z) = \frac{2(z - a_k(t))}{b_k(t) - a_k(t)} - 1 \tag{36}$$

This allows to define the problem on $[-1,1]$ instead of $[a_k, b_k]$. Under this change of variables, the variational formulation takes the form:

$$\int_{-1}^{1} \rho_k c_k \left[\frac{\partial T_k}{\partial t} + \frac{\partial \bar{z}}{\partial t}\frac{\partial T_k}{\partial \bar{z}}\right] \bar{v} \frac{b_k - a_k}{2} \, d\bar{z} - \int_{-1}^{1} \lambda_k \frac{\partial^2 T_k}{\partial \bar{z}^2} \bar{v} \frac{2}{b_k - a_k} d\bar{z} = 0 \tag{37}$$

The third step is the discretization of (35) in a subspace of finite dimension. Let $E_n = (\Psi_j)_{j=1}^n$ be a set a linearly independent functions. The temperature field is projected onto this subspace:

$$\forall t \geq 0, \forall \bar{z} \in]-1,1[,\ T_k(t,\bar{z}) = \sum_{j=1}^{n} \theta_{k,j}(t)\Psi_j(\bar{z}) \tag{38}$$

Then one can project the equation (35) onto E_n. This yields, $\forall i = 1,\dots,n$:

$$\begin{array}{rcl} \rho_k c_k \sum\limits_{j=1}^{n} \int_{-1}^{1} \left[\dot{\theta}_{k,j}\Psi_j(\bar{z}) + \frac{\partial \bar{z}}{\partial t}\theta_{k,j}\Psi_j'(\bar{z})\right]\Psi_i(\bar{z})\frac{b_k-a_k}{2}\,d\bar{z} & & \\ -\frac{2\lambda_k}{b_k-a_k}\sum\limits_{j=1}^{n}\int_{-1}^{1}\frac{\partial^2}{\partial \bar{z}^2}\left[\theta_{k,j}\Psi_j(\bar{z})\right]\Psi_i(\bar{z})d\bar{z} & = & 0 \end{array} \tag{39}$$

By developing this expression and using integration by parts for the second term, one gets:

$$\begin{array}{lllll} \rho_k c_k \sum\limits_{j=1}^{n}\left\{\dot{\theta}_{k,j}\dfrac{b_k-a_k}{2}\displaystyle\int_{-1}^{1}\Psi_j(\bar{z})\Psi_i(\bar{z})\,d\bar{z}\right\} & + & \rho_k c_k \sum\limits_{j=1}^{n}\left\{\theta_{k,j}\displaystyle\int_{-1}^{1}\left(\Psi_j'(\bar{z})\frac{\partial\bar{z}}{\partial t}\right)\Psi_i(\bar{z})\,\frac{b_k-a_k}{2}\,d\bar{z}\right\} & & \\ -\left[\dfrac{2\lambda_k}{b_k-a_k}\sum\limits_{j=1}^{n}\theta_{k,j}\Psi_j'(\bar{z})\Psi_i(\bar{z})\right]_{\bar{z}=-1}^{1} & + & \dfrac{2\lambda_k}{b_k-a_k}\sum\limits_{j=1}^{n}\left\{\theta_{k,j}\displaystyle\int_{-1}^{1}\Psi_j'(\bar{z})\Psi_i'(\bar{z})\,d\bar{z}\right\} & = & 0 \end{array} \tag{40}$$

By using this procedure one obtains the following matrix expression (details can be found in [7, p.78]):

$$\rho_k c_k\left(\frac{b_k-a_k}{2}\mathbf{A}\dot{\boldsymbol{\theta}}_k - \tfrac{1}{2}\left[(\dot{a}_k+\dot{b}_k)\boldsymbol{\Pi}+(\dot{b}_k-\dot{a}_k)\boldsymbol{\Gamma}\right]\boldsymbol{\theta}_k\right) + \frac{2\lambda_k}{b_k-a_k}\boldsymbol{\Lambda}\boldsymbol{\theta}_k = \mathbf{f}_k(\boldsymbol{\theta}_k) \tag{41}$$

where

$$\left\{\begin{array}{rcl} \boldsymbol{\theta}_k &=& (\theta_{k,1}\dots,\theta_{k,n})^T \\ A_{ij} &=& \displaystyle\int_{-1}^{1}\Psi_j(\bar{z})\Psi_i(\bar{z})\,d\bar{z} \\ \Lambda_{ij} &=& \displaystyle\int_{-1}^{1}\Psi_j'(\bar{z})\Psi_i'(\bar{z})\,d\bar{z} \\ \Pi_{ij} &=& \displaystyle\int_{-1}^{1}\Psi_j'(\bar{z})\Psi_i(\bar{z})\,d\bar{z} \\ \Gamma_{ij} &=& \displaystyle\int_{-1}^{1}\bar{z}\Psi_j'(\bar{z})\Psi_i(\bar{z})\,d\bar{z} \\ f_{k,i}(\boldsymbol{\theta}_k) &=& \dfrac{2\lambda_k}{b_k-a_k}\displaystyle\sum_{j=1}^{n}\theta_{k,j}\Psi_j'(1)\Psi_i(1) - \dfrac{2\lambda_k}{b_k-a_k}\sum_{j=1}^{n}\theta_{k,j}\Psi_j'(-1)\Psi_i(-1) \end{array}\right. \tag{42}$$

Note that the matrices $\mathbf{A}$, $\boldsymbol{\Pi}$, $\boldsymbol{\Gamma}$ and $\boldsymbol{\Lambda}$ only depend on the functions Ψ_j. So as to reduce the computational cost they are evaluated once at the beginning of the computation. Moreover, $f_{k,i}(\boldsymbol{\theta}_k)$ is computed using the boundary conditions.

Finally, the functions Ψ_j remain to be chosen. In this work polynomial functions are considered. They are chosen so that the first and second degree of freedom yield the value of the temperature at the lower and upper boundaries respectively. In addition they are constructed so as to be orthonormal. The constructions of those polynomials reads:

1. $\forall x \in [-1,1],\ \Psi_1(x) = \dfrac{1-x}{2},\ \Psi_2(x) = \dfrac{1+x}{2}$
2. For $i \geq 3$, Ψ_i is the polynomial of degree $i-1$ such that
   (a) $\Psi_i(-1) = \Psi_i(+1) = 0$

(b) $\int_{-1}^{1} \left(\Psi_i(\bar{z})\right)^2 d\bar{z} = 1$

(c) $\int_{-1}^{1} \Psi_i(\bar{z})\Psi_j(\bar{z}) d\bar{z} = 0, \quad \forall j = 3, \ldots, i-1$

One may note that conditions 1. and 2.(a) allow to easily manage a Dirichlet boundary condition since $T_k(a_k) = \theta_{k,1}$ and $T_k(b_k) = \theta_{k,2}$.

4.2. Implicit time marching algorithm

To insure robustness and a lower computational cost, an implicit Euler time marching scheme is used. The time interval is discretized into N_t discrete instants and superscript n is used to denote the n-th time step.

Let's assume that the computational domain has been split into N_x cells (as illustrated in Figure 4). Then, for a given cell k in mode md, the general shape of equation to solve to go from time step n to time step $n+1$ reads:

$$\boldsymbol{M}_{md} \frac{\mathbf{U}_k^{n+1} - \mathbf{U}_k^n}{\Delta t} + \boldsymbol{G}_{md}(\mathbf{U}_L^{n+1}, \mathbf{U}_k^{n+1}, \mathbf{U}_R^{n+1}) = \boldsymbol{S}_{md}(\mathbf{U}_k^{n+1}) \tag{43}$$

where for all $k \in [\![1, N_x]\!]$, the unknown vector is denoted $\mathbf{U}_k^{n+1}$. As an example, in the glaze mode, $\mathbf{U}_k^{n+1} = (h_f, h_i, \theta_{i,1}, ..., \theta_{i,ng})$ (where ng is the number of degrees of freedom of the Galerkin method). Subscripts L and R denote the left and the right neighbouring cells of cell k, respectively. $\boldsymbol{G}_{md}$ is a non-linear function defined by the spatial discretization of the running liquid film (Roe finite volume scheme). Finally, $\boldsymbol{S}_{md}$ is a local function (it only depends on the variable inside the local cell) which models heat transfer in the normal direction including phase change as well as source terms (previously described Galerkin method). It is worth noting that the dimension of $\mathbf{U}_k^{n+1}$ depends on k, md and n since layers may appear or disappear during a time step.

There are two main difficulties in the construction of the implicit method. First, as all the cells of the mesh are coupled with their left and right neighbouring cells through the running liquid film, it is complicated to devise a global implicitation of the method (i.e. a method which would simultaneously yield $\mathbf{U}_k^{n+1}$ in every cell). To overcome this problem, a fixed point algorithm is used. The general idea is to perform a local implicitation and iterate over the cells until convergence so as to construct a sequence $\left(\left\{\mathbf{U}_k^{(l)}\right\}_{k\in[\![1,N_x]\!]}\right)_l$ that converges to $\left(\left\{\mathbf{U}_k^{n+1}\right\}_{k\in[\![1,N_x]\!]}\right)$. More precisely, the first step is to chose a numbering for iterating over the cells. In order to enhance convergence, the idea is to run through the cells in the direction of propagation of information. It is given by the direction of shearing of the film, which determines the main direction of propagation of the film downstream. For the present targeted icing applications, the numbering starts at the stagnation point (in red in Figure 4). Then one firstly numbers the lower surface and then the upper one, as illustrated in Figure 4. The left and right neighbouring cells relative to a given cell k are defined with respect to this numbering direction.

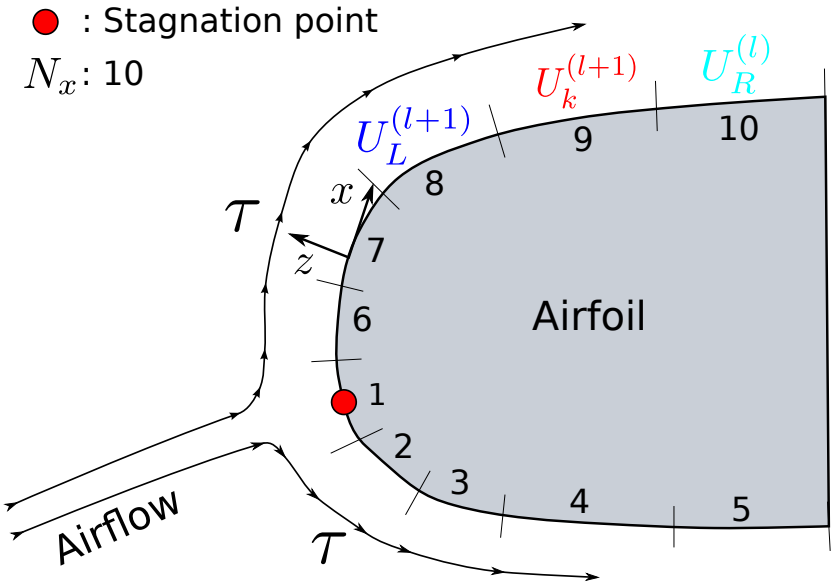

Figure 4: Illustration of the numerical discretization into N_x cells (in this illustration $N_x = 10$. The optimal numbering is performed according to the shearing directions (direction of propagation of information downstream). The red dot denotes the stagnation point

The sequence is then initialized using the values $\mathbf{U}_k^n$:

$$\mathbf{U}_k^{(0)} = \mathbf{U}_k^n \quad , \quad k \in [\![1, N_x]\!] \tag{44}$$

On both parts (upper and lower) the iterative process proceeds from downstream. At a given cell k, $\mathbf{U}_L^{(l+1)}$ is know, while $\mathbf{U}_R^{(l+1)}$ is not. $\mathbf{U}_k^{(l+1)}$ is computed using $\mathbf{U}_L^{(l+1)}$ and $\mathbf{U}_R^{(l)}$ using equation (45).

$$\boldsymbol{M}_{md} \frac{\mathbf{U}_k^{(l+1)} - \mathbf{U}_k^n}{\Delta t} + \boldsymbol{G}_{md}\left(\mathbf{U}_L^{(l+1)}, \mathbf{U}_k^{(l+1)}, \mathbf{U}_R^{(l)}\right) = \boldsymbol{S}_{md}\left(\mathbf{U}_k^{(l+1)}\right) \tag{45}$$

The second difficulty is to manage the appearance or disappearance of a layer and the switching between modes. In a given mode md, solving equation (45) may yield a solution $\mathbf{U}_k^{(l+1)}$ which is incompatible with this mode. For example, assume the cell is in a rime mode at t^n and that solving equation (45) yields $T_i^{(l+1)}(z = 0) > T_m$. This solution is clearly incompatible with the rime mode. Indeed, it means that the ice should be melting and that a liquid layer should appear. Hence the mode of the cell at iteration $(l + 1)$ can't be rime. The mode at iteration $(l + 1)$ should be changed and the corresponding equation (45) should be solved (and so on until one finds a compatible mode). In a more general way, the trial process of different modes is illustrated in Figure 5.

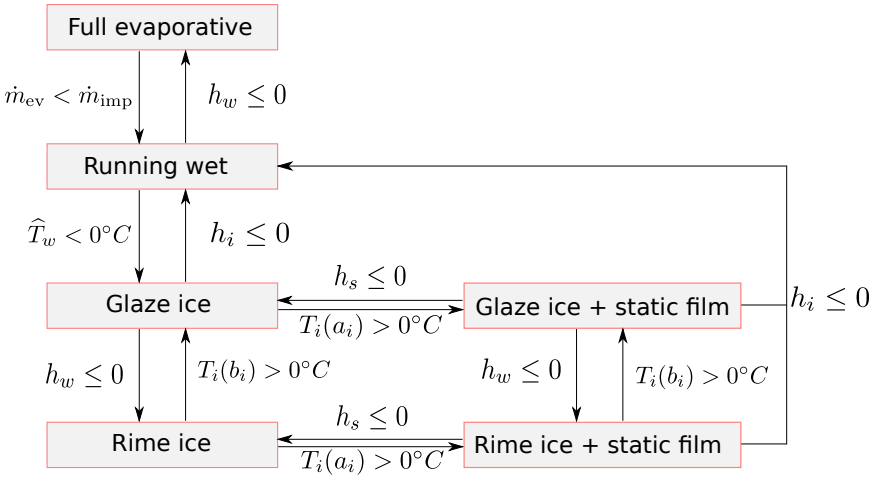

Figure 5: Illustration of the trial process during implicit time marching. A mode is assumed and the resulting solution is checked for consistency

These considerations lead to the formulation of the following algorithm:

[Initializing using values at the previous time step]
For k **from** 1 **to** N_x **do**
  $\mathbf{U}_k^{(0)} \leftarrow \mathbf{U}_k^n$
end For
$l \leftarrow -1$
Repeat
  $l \leftarrow l + 1$
  [Loop on control volumes]
  For k **from** 1 **to** N_x **do**
    Assume cell is in same mode md as at previous time step
    Repeat
      solve the equation

$$\boldsymbol{M}_{md} \frac{\mathbf{U}_k^{(l+1)} - \mathbf{U}_k^n}{\Delta t} + \boldsymbol{G}_{md}\left(\mathbf{U}_L^{(l+1)}, \mathbf{U}_k^{(l+1)}, \mathbf{U}_R^{(l)}\right) = \boldsymbol{S}_{md}\left(\mathbf{U}_k^{(l+1)}\right) \tag{46}$$

      If ($\mathbf{U}_k^{(l+1)}$ is not a compatible mode (as defined by Figure 5)) **then**
        Change mode according to Figure 5 and solve (46) again
      end If

    until (Compatible mode is found)
  end For
until $(\forall k \in [\![1, N_x]\!], \left\| \frac{\mathbf{U}_k^{(l+1)} - \mathbf{U}_k^{(l)}}{\mathbf{U}_k^{(l+1)}} \right\| < \varepsilon)$

Algorithm 1: Fixed point for the implicitation of time integration

5. Validation: The Stefan Problem

In this section, a Stefan problem [2] is considered so as to assess and validate the Galerkin method. Consider a block of ice, initially at $250K$, as in Figure 6. The block is heated for $5\,s$ from beneath with an imposed temperature of $T_L = 300\,K$. As the imposed temperature is greater than the melting temperature ($273.15K$) the block of ice will undergo a solid-liquid phase change and a melting front will propagate from beneath.

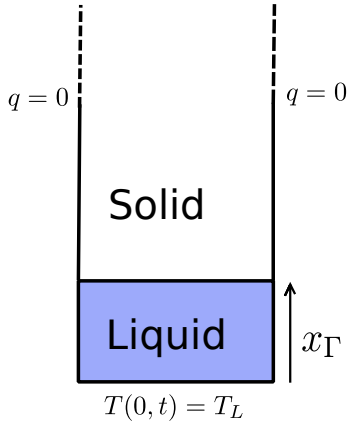

Figure 6: Illustration of the one dimensional Stefan problem: a block of ice is heated from beneath at a temperature T_L. Both lateral sides are adiabatic ($q = 0$).

For a semi-infinite block, this problem has an analytical solution [2]. However, when performing the numerical simulation, the ice block has a finite size. Therefore, the length of the block is taken large enough so that the main heat transfer is confined to the bottom of the domain. In the present case the length of the block is $0.01m$. The physical properties used for this case are given in table 1.

$c_s\ (J.kg^{-1}.K^{-1})$	$c_l\ (J.kg^{-1}.K^{-1})$	$L_f\ (J.kg^{-1})$	$\lambda_s\ (W.m^{-1}.K^{-1})$	$\lambda_l\ (W.m^{-1}.K^{-1})$	$T_m\ (K)$
2060	4185	330000	2.1	0.6	273.15

Table 1: Physical properties of ice used for solving the Stefan problem

The previously described method is used to solve the Stefan problem. Therefore, the initial mode is "rime". When the melting front starts to propagate, the mode switches to "rime with static film". The problem is solved using 2, 4, 6 and 8 degrees of freedom in the Galerkin expansion and a time step of $0.01s$. Figure 7a shows the melting front position as a function of time. With 2 degrees of freedom, the numerical solution is overestimated. The solution is improved with increasing number of degrees of freedom. With 4 or more degrees of freedom the results are in good agreement with the analytical solution.

In addition, Figure 7b shows the sensitivity of the solution obtained with 8 degrees of freedom to the time step. The agreement with the analytical solution is very good. The solution obtained with $\Delta t = 0.1s$ is slightly less accurate. Solutions obtained with $\Delta t = 0.01s$ and $\Delta t = 0.001s$ are almost identical.

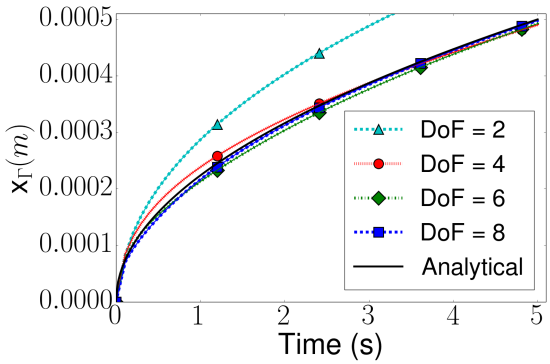

(a) Comparison between the analytical solution and numerical solutions obtained with increasing number of degrees of freedom (fixed time step $\Delta t = 0.01s$)

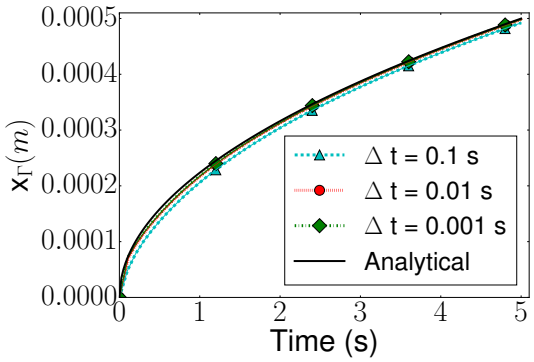

(b) Comparison between the analytical solution and numerical solutions obtained with different time steps (fixed DoF=8)

Figure 7: Melting front position as a function of time

So as to get a better idea of the validity of the method, one may also compare the numerical and analytical temperature fields. Here, the temperature fields are compared at the very first instants of the melting front propagation ($t = 0.1s$) and at a later time ($t = 5s$). As shown in Figure 8b, at $t = 5s$, except when using only 2 degrees of freedom, the agreement between analytical and numerical solutions is excellent. However, Figure 8a shows that at $t = 0.1s$, the numerical temperature fields tend to oscillate. This is due to the truncation operated by the Galerkin procedure. These oscillations tend to be lessened when a higher number of degrees of freedom is used. With 8 degrees of freedom, the results are in good agreement with the analytical solution. In the rest of this work, 8 degrees of freedom will be used for the Galerkin method.

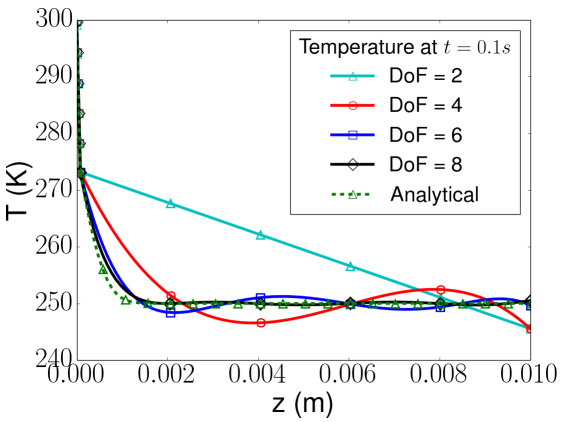

(a) Temperature profile at $t = 0.1s$

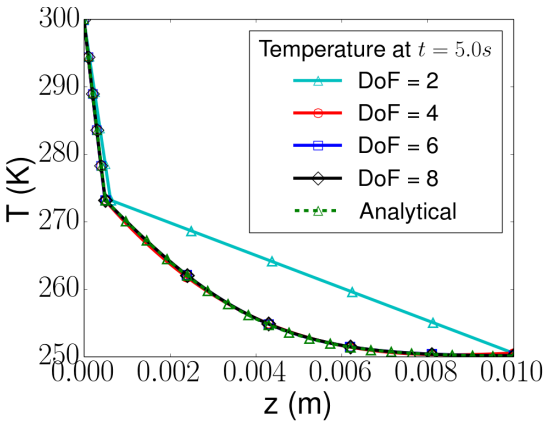

(b) Temperature profile at $t = 5s$

Figure 8: Temperature field: comparison between analytical and numerical solutions obtained with increasing number of degrees of freedom

6. Ice Accretion Cases

This section describes the results obtained for two steady ice accretion cases (rime and glaze). They are compared with ice shapes predicted with Messinger's method (implemented in the module MESSINGER2D of the ONERA icing tool IGLOO2D [22], the present method is implemented in MiLeS2D). In both cases, the airfoil is discretized using 128 points.

The icing conditions for both cases are given in Table 2. Rime icing conditions correspond to the case where the external temperature is well below $273.15K$. In this case the supercooled droplets freeze almost instantly upon impacting the surface. Therefore in rime conditions, there is no water running back. In glaze icing conditions, the external temperature is below but closer to $273.15K$. In this case, the droplets start to freeze upon impact but a certain amount of water runs back downstream.

Case	Airfoil	Chord	α (°)	P_∞ (Pa)	T_∞ (K)	M_∞	rH_∞	TWC $(g.m^{-3})$	MVD (μm)
Rime	NACA0012	0.5334	4	101325	256.8	0.321	1	0.34	20
Glaze	GLC305	0.9144	1.5	101325	263.15	0.395	1	0.54	20

Table 2: Aerodynamic and atmospheric conditions for the rime and glaze icing cases. The droplet size distribution is assumed to be monodisperse

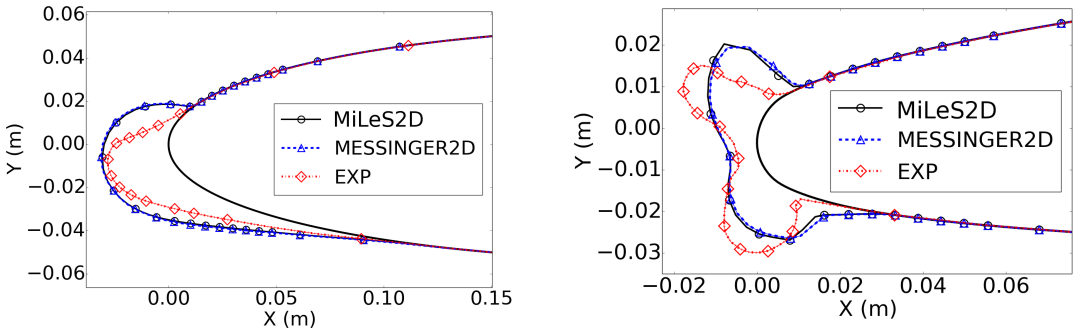

(a) Rime ice shape (accretion time: 690s)

(b) Glaze ice shape (accretion time: 360s

Figure 9: comparison between MiLeS2D, MESSINGER2D and experimental data for rime and glaze cases

Figure 9 shows that the ice shapes predicted with MiLeS2D and MESSINGER2D match very well. This section shows that in steady icing conditions, the present numerical methodology is able to predict the same results as Messinger's method. This section therefore provides a successful benchmark (for steady configurations) for MiLeS2D before performing a case for which the method is really designed (unsteady and heated leading edge).

7. Delayed Activation With Runback

We now proceed to show that the method is also able to treat unsteady situations of high interest for icing applications, which can't be treated with Messinger's approach.

Consider the glaze icing conditions of table 3 and assume that after $20s$ of accretion, an ice protection system is activated. The heat provided by the system is represented by an internal heat transfer coefficient of $1500W.K^{-1}.m^{-2}$ and an internal temperature of $323.15K$. The system is active between $s = -0.015m$ and $s = 0.015m$. This corresponds to an illustrative case of delayed activation. Some ice has already had the time to build up and an internal heating will be activated to eliminate it. Such a case can't be simulated using Messinger's approach. Indeed, it can't account for the dynamics of the melting process nor can it account for the dynamics of the running back water film created when all the ice is melted.

Airfoil	Chord	α (°)	P_∞ (Pa)	T_∞ (K)	M_∞	rH_∞	TWC $(g.m^{-3})$	MVD (μm)
NACA0012	0.5334	4	101325	263.15	0.321	1	0.34	20

Table 3: Aerodynamic and atmospheric conditions for the delayed activation case. The droplet size distribution is assumed to be monodisperse

7.1. Step 1: ice build up

During the first $20s$ of the case the internal heating is not activated. Unsteady phenomena occur during this step but only at the very beginning of the build up process.

Figure 10 shows, at $t = 0.25s$, the liquid running film and ice thickness as well as the droplet impact rate as functions of the curvilinear abscissa. Different areas of accretion mode (rime or glaze) are visible. Between approximately $s = -0.01m$ and $s = 0.0m$ droplets are impacting, ice is building up and a liquid film is flowing on top (glaze mode). On the other hand, for $s < -0.02m$ or in the neighborhood of $s = 0.0m$, ice is building-up in rime mode.

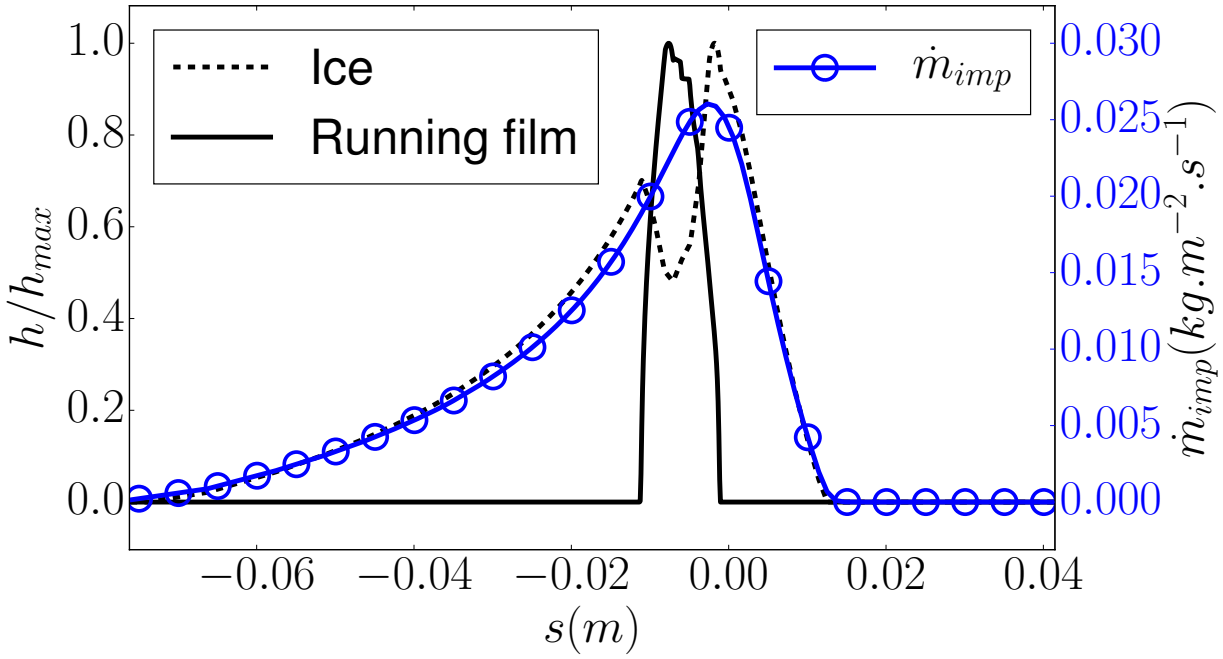

Figure 10: Droplet impact rate, running film and ice build up modes at $t = 0.25s$. The plotted thicknesses dimensionless. The maximum thicknesses are $h_{rf,max} = 1.9\,\mu m$ for the running film and $h_{i,max} = 6.9\,\mu m$ for the ice.

As shown in Figure 11 the film flows downstream under the effect of the aerodynamic forces. The film flows into regions where ice was growing in rime mode. Therefore the build up process changes downstream as the liquid film runs back and flows over the ice. Regions which initially started in rime mode switch to glaze mode. In addition, note that after $t = 1s$ steady state is reached regarding the runback of the liquid film (whereas ice continues to grow). This unsteady process occurs only during the first instants of the build up process.

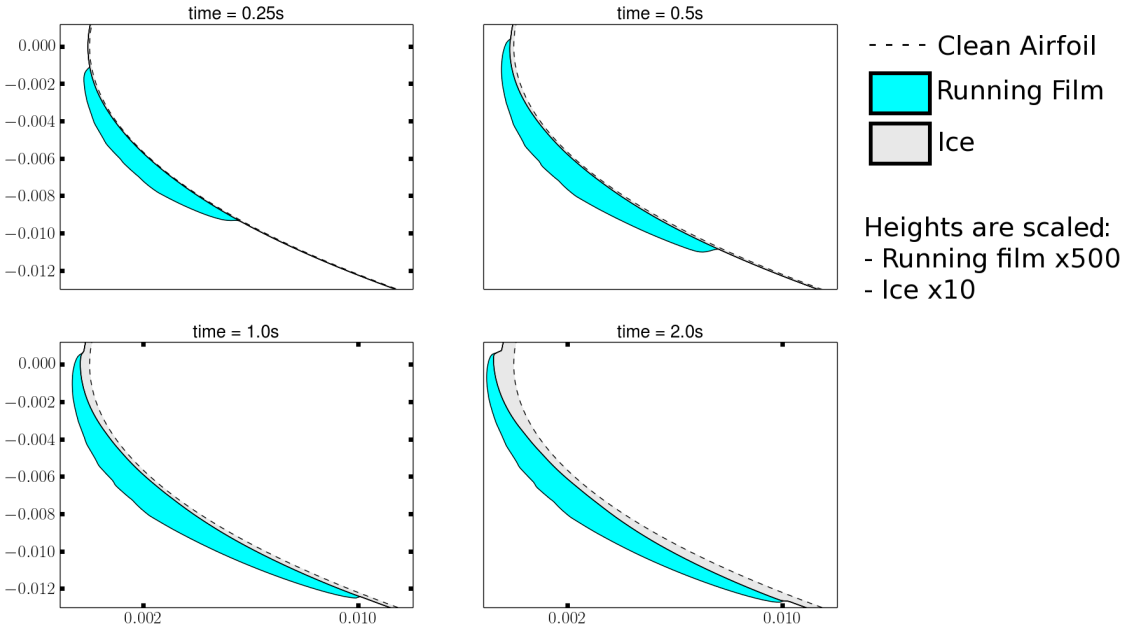

Figure 11: Unsteady runback process during first instants of the simulation

As shown in Figure 12, this leads to build up of ice at the leading edge. After $20s$ the maximal ice thickness is of $0.84mm$. From this point on a heating term is activated in the red dotted region. Note that for representation reasons the dotted region is not plotted exactly at the boundary. However, it is indeed at the upper boundary of the airfoil that the heating term in applied. That is to say, the heating term is directly applied as a (lower) boundary condition of the triple layer model.

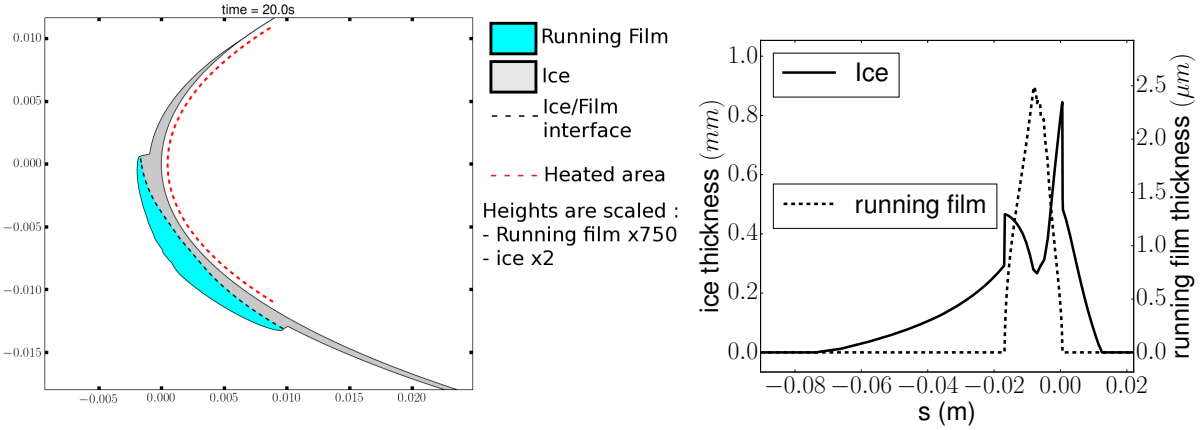

(a) Two dimensional view of the ice shape and running film. (b) Thickness of ice layer and running film layer.

Figure 12: Ice shape at $t = 20s$

7.2. Step 2: activation of heating

At $t = 20s$ the internal heating is activated. The layer of ice starts to melt. Figure 13 shows the temperature field in the ice block at the stagnation point just after the internal heating is applied. The melting front propagates and a temperature gradient is clearly visible.

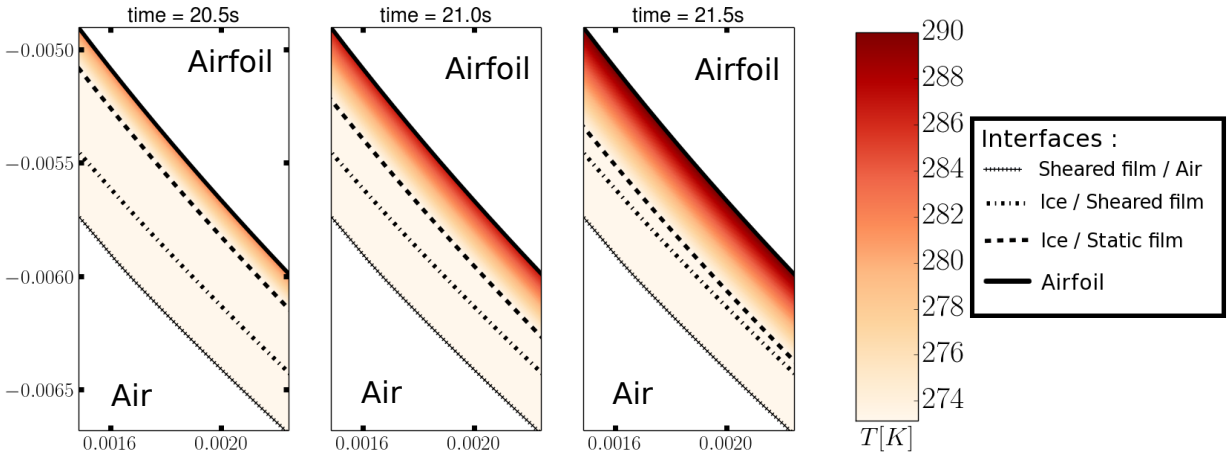

Figure 13: Temperature field in the ice block near the leading edge. A temperature gradient is clearly visible as the melting front propagates. The dashed line represents the melting front. The film height is scaled x50

Figure 14a shows the temperature profile and the position of the melting front along the normal direction to the stagnation point. The temperature gradient is clearly visible. The ice melting process is also visible in Figure 14b. The ice thickness decreases as it melts and is replaced by a layer of static film. Once the ice layer has completely melted the static layer comes into contact with the running film layer. At this point the mode switches to "running wet" and the whole thickness of the static layer is transferred to the dynamic layer. The dynamic layer is then very rapidly evacuated downstream and returns to its steady thickness.

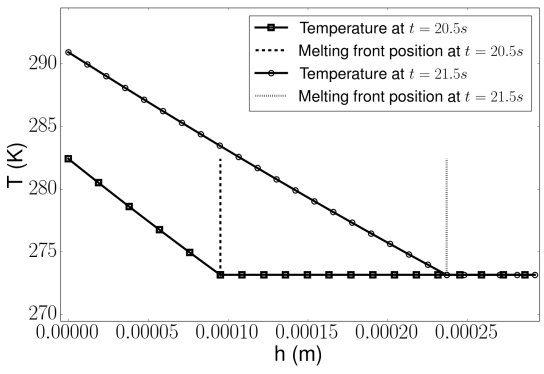

(a) Temperature profile in the normal direction at the leading edge

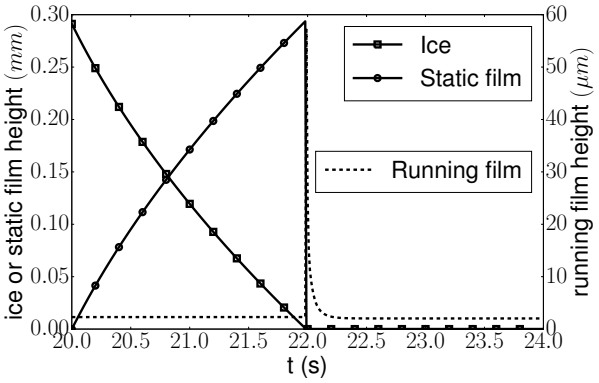

(b) Thicknesses as function of time

Figure 14: Temperature field and layer thicknesses during the melting process

In addition, during the unsteady melting process, small region of melted water are released and flow downstream, as shown in Figure 15. The whole process occurs as follows:

- $t = 20.03s$: in a given cell at the end of the ice block, once the melting front has propagated through the whole thickness of ice, the local mode switches to 'running wet'.

- $t = 20.08s$: The liquid water comes into contact with the external flow field. The liquid film runs back downstream under the effect of the aerodynamic forces.
- $t = 20.21s$: however, as the liquid leaves the protected area, it is no longer heated enough. It starts to freeze under the effect of the cold external conditions.
- $t = 20.3s$: therefore, a small ice ridge starts build up outside of the heated area.

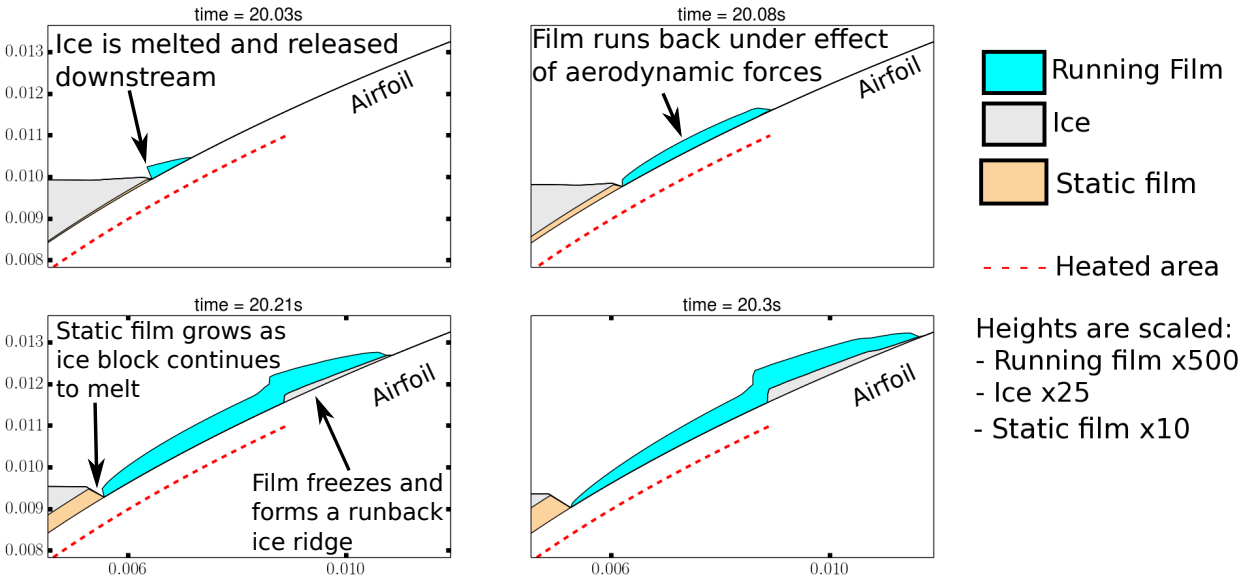

Figure 15: A small region of ice is melted. The resulting liquid water runs downstream.

7.3. Step 3: formation of ice ridges

After $10s$ of internal heating, the protected area is free from ice. The internal heating manages to keep the leading edge free of ice. However it is not sufficient to be fully evaporative. Figure 16 shows the predicted ice shapes after $50s$. The temperature field in the running liquid film is shown. The water is heated along the protected area. However, once the water exits the protected area, the cold external conditions rapidly lead to freezing. Therefore the water runs back and freezes further downstream, generating two runback ice ridges, one on the pressure side and the other on the suction side.

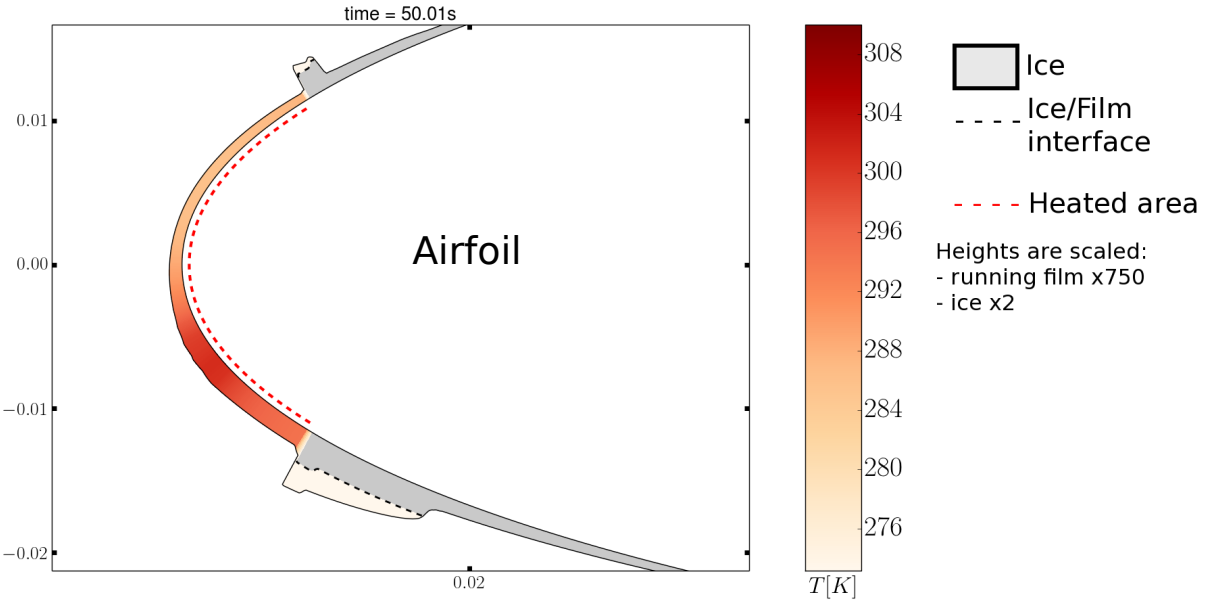

Figure 16: Predicted runback ice shapes after $50s$ (obtained with a mesh size of $\Delta s = 0.0001m$)

7.4. Mesh convergence analysis

All the previous results where obtained with a mesh size of $\Delta s = 0.0001m$. This choice was the result of a mesh refinement analysis. Figure 17 shows a clear effect of mesh refinement on the runback shapes. Indeed, for a coarse mesh, the runback ice shapes appear to be more smoothed out. Mesh refinement has the effect of sharpening the ice shapes.

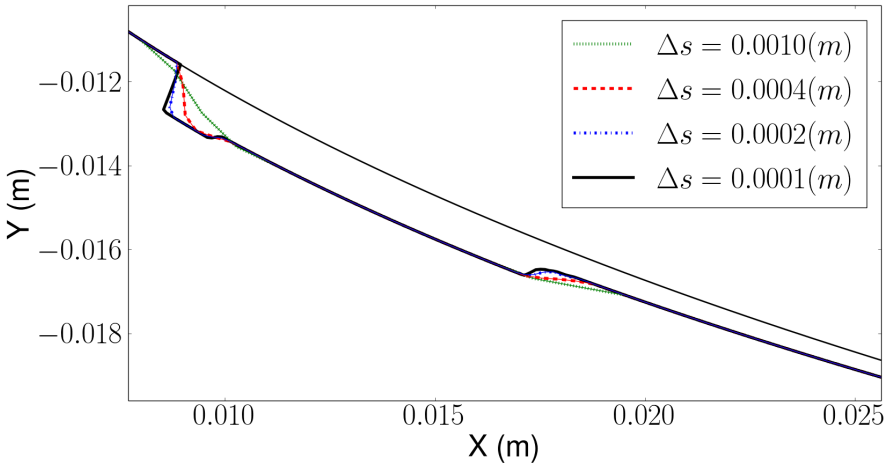

(a) Upper ridge

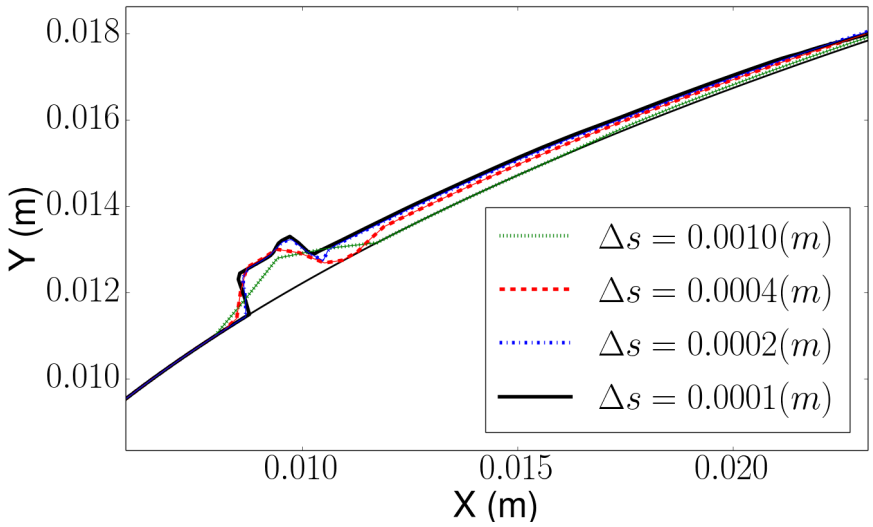

(b) Lower ridge

Figure 17: Runback ice shapes: effect of mesh refinement

8. Conclusion and Perspectives

In this paper, a three-layer model for the simulation of unsteady icing phenomena was proposed. The methodology models the dynamics of the sheared liquid film with a lubrication assumption. The heat equation is used to model heat transfer in the normal direction in the static layers. Moreover the dynamics of the melting front is taken into account with a Stefan condition. The heat and mass transfer equations for the running liquid film are solved using a Roe scheme. In the static layers, a Galerkin finite element method is used to solve the heat equation and treat the Stefan condition. These spatial discretization schemes are embedded into an implicit time marching scheme.

The approach was shown to give good results when compared to analytical solutions for a one dimensional Stefan problem. It was shown that the melting front and temperature fields could be well predicted.

Secondly, two ice accretion cases where simulated. The results were compared to those obtained with Messinger's method and to experimental data. In both cases, rime and glaze icing conditions, the present

method predicted the same results as Messinger's approach. However, the results were also in poor agreement with the experimental data. In order to overcome this drawback, a possible line of improvement would be to update the aerodynamic field and droplet impingement data. As the present method is fully unsteady, one could update the aerodynamic field and droplet impingement data in a consistent way.

Finally, the capabilities of the method to treat unsteady cases was demonstrated. A situation of delayed system activation was considered. Indeed, it is to deal with such unsteady cases that the present method was developed. The results may be summed up in three steps. Firstly, ice builds up. Secondly, a system is activated (modelled by an internal heating). The method predicted the propagation of the melting front inside the ice block. Moreover, the associated temperature gradient was clearly visible. Thirdly, once the ice block at the leading edge was melted, water flowed downstream. Once out of the heated area, the water began to freeze, creating two ridges of runback ice, one on the suction side, another on the pressure side. It is worthwhile to note that Messinger's method is unable to account for such phenomena as it is based on steady state assumptions. The lack of experimental data and its high scatter does not at present time allow for a full validation of the model. However, ongoing research projects aim to fill the experimental data gap.

With these results at hand, the next step is to couple this methodology with a solver for an electro-thermal ice protection system [8]. Moreover, combining them with recent work on ice shedding mechanisms [5, 4] would enable the simulation of a full de-icing cycle.

Bibliography

[1] KM Al-Khalil, TG Keith Jr, and KJ De Witt. Further development of an anti-icing runback model. *AIAA Paper*, 266, 1991. 3

[2] V. Alexiades and A.D. Solomon. *Mathematical Modeling of Melting and Freezing Processes*. Hemisphere, 1993. 15

[3] L Bennani. *Two dimensional modelling of electrothermal ice protection systems*. PhD thesis, ISAE, 2014. 25

[4] L. Bennani, P. Villedieu, and M. Salaun. A mixed adhesion–brittle fracture model and its application to the numerical study of ice shedding mechanisms. *Engineering Fracture Mechanics*, 158:59–80, 2016. 24

[5] L. Bennani, P. Villedieu, M. Salaun, and P. Trontin. Numerical simulation and modeling of ice shedding: Process initiation. *Computers & Structures*, 142(0):15 – 27, 2014. 24

[6] Y. Bourgault, H. Beaugendre, and W.G. Habashi. Development of a shallow-water icing model in fensap-ice. *Journal of Aircraft*, 37(4):640–646, 2000. 3

[7] R. Chauvin. *Un modèle unifié pour les phénomènes de givrage en aéronautique et les systèmes de protection thermiques*. PhD thesis, ISAE, 2015. 5, 6, 7, 11

[8] R. Chauvin, P. Villedieu, and P. Trontin. A robust coupling algorithm applied to thermal ice protection system unsteady modeling. In *6th AIAA Atmospheric and Space Environments Conference*, page 2061, 2014. 24

[9] T. H. Chilton and A. P. Colburn. Mass transfer (absorption) coefficients prediction from data on heat transfer and fluid friction. *Industrial & engineering chemistry*, 26(11):1183–1187, 1934. 7

[10] G. Gomez de Segura Solay, E. Radenac, R. Chauvin, and C. Laurent. Simulations of ice accretion, runback and droplet re-emission in a multi-stage model of aeronautical engine. In *8th AIAA Atmospheric and Space Environments Conference*, page 4350, 2016. 3

[11] G Gori, M Zocca, M Garabelli, A. Guardone, and G. Quaranta. Polimice: A simulation framework for three-dimensional ice accretion. *Applied Mathematics and Computation*, 267:96–107, 2015. 3

[12] H. Beaugendre, F. Morency, W. G. Habashi. FENSAP-ICE's three-dimensional in-flight ice accretion module: ICE3D. *Journal of Aircraft*, 40(2):239–247, 2003. 3

[13] I. Paraschivoiu, F. Saeed. Ice accretion simulation code canice. In *Proceedings of the International Areospace Symposium carafoli*, pages 81–86, 2001. 3

[14] J. E. Dillingh, H. M. W. Hoeijmakers. Simulation of ice accretion on airfoils during flight. Technical report, SAE Technical Paper, 2003. 3

[15] B. Larrouturou. How to preserve the mass fractions positivity when computing compressible multi-component flows. *Journal of Computational Physics*, 95(1):59–84, 1991. 10

[16] P. Lavoie, S. Bourgault-Côté, and E. Laurendeau. Numerical algorithms for infinite swept wing ice accretion. *Computers & Fluids*, 161:189–198, 2018. 3

[17] B. L. Messinger. Equilibrium temperature of an unheated icing surface as a function of air speed. *Journal of the Aeronautical Sciences*, 20:29–42, 1953. 3

[18] T.G. Myers and D.W. Hammond. Ice and water film growth from incoming supercooled droplets. *International Journal of Heat and Mass Transfer*, 42(12):2233–2242, 1999. 3

[19] TG Myers, SL Mitchell, G Muchatibaya, and MY Myers. A cubic heat balance integral method for one-dimensional melting of a finite thickness layer. *International Journal of Heat and Mass Transfer*, 50(25):5305–5317, 2007. 3

[20] Tim G Myers. Extension to the messinger model for aircraft icing. *AIAA journal*, 39(2):211–218, 2001. 3

[21] S.P. Otta and A.P. Rothmayer. Instability of stagnation line icing. *Computers & Fluids*, 38(2):273–283, 2009. 3

[22] P. Trontin and G. Blanchard and A. Kontogiannis and P. Villedieu. Description and assessment of the new onera 2d icing suite igloo2d. In *9th AIAA Atmospheric and Space Environments Conference-AVIATION*, 2017. 4, 16
[23] R. W. Gent. TRAJICE2-A combined water droplet trajectory and ice accretion prediction program for aerofoils. *RAE TR*, 90054, 1990. 3
[24] E. Radenac. Validation of a 3d ice accretion tool on swept wings of the sunset2 program. In *8th AIAA Atmospheric and Space Environments Conference*, page 3735, 2016. 4
[25] P. L. Roe. Approximate riemann solvers, parameter vectors, and difference schemes. *Journal of computational physics*, 43(2):357–372, 1981. 10
[26] T. Hedde, D. Guffond. ONERA three-dimensional icing model. *AIAA journal*, 33(6):1038–1045, 1995. 3
[27] JC Tsao and AP Rothmayer. Application of triple-deck theory to the prediction of glaze ice roughness formation on an airfoil leading edge. *Computers & fluids*, 31(8):977–1014, 2002. 3
[28] J.C Tsao, A.P. Rothmayer, and A.I. Ruban. Stability of air flow past thin liquid films on airfoils. *Computers & fluids*, 26(5):427–452, 1997. 3
[29] P. Verdin, J.P.F. Charpin, and C.P. Thompson. Multistep results in icecremo2. *Journal of Aircraft*, 46(5):1607–1613, 2009. 3
[30] W. L. Smith. Weather Problems Peculiar to the New York-Chicago Airway. *Monthly Weather Review*, 57:503–506, December 1929. 2
[31] W. M. Leary. We Freeze to Please: A History of NASA's Icing Research Tunnel and the Quest for Flight Safety. The NASA History Series, 2002. 2
[32] W. Wright. *User's Manual for LEWICE Version 3.2*, 2008. 3
[33] D. Yanxia, G. Yewei, X. Chunhua, and Y. Xian. Investigation on heat transfer characteristics of aircraft icing including runback water. *International Journal of Heat and Mass Transfer*, 53(19-20):3702–3707, 2010. 3

Appendix A. Neglecting the tangential heat fluxes in the ice and static film layers: approximation assessment

In the model presented previously,heat conduction is considered in the normal direction only. So as to assess this approximation, consider the case illustrated in Figure A.18 where an internal heating is applied to a specific region of an ice block. This case is simulated with an in-house code that solves the two dimensional heat transfer problem with phase change using an enthalpy method [3]. This way, the temperature gradient can be computed.

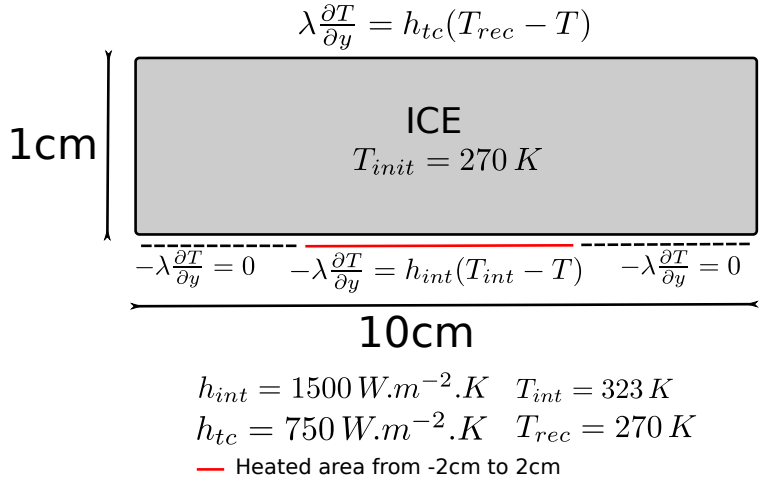

Figure A.18: Two dimensional case

In addition, Figure A.19 shows that the x component of the temperature gradient is non zero only in a confined region at the edge of the heated area, whereas variations in the y direction are much more present. The arrows representing the temperature gradient show that it is mainly normal to the boundary.

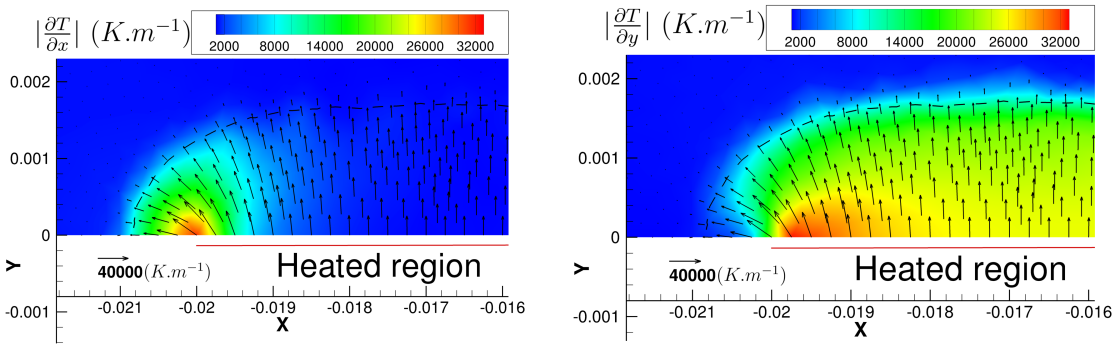

(a) $|\frac{\partial T}{\partial x}|$ (b) $|\frac{\partial T}{\partial y}|$

Figure A.19: Comparison between x and y components of the temperature gradient at $t = 30s$. Arrows represent $-\nabla T$. The dashed line represents the position of the melting front.

Therefore, although the x component is not zero strictly speaking, not taking it into account is a reasonable approximation. This allows to reduce the phase change problem to one dimension and to construct a model that retains the relevant physics while being much cheaper computationally.